

GeSn (0.524 eV) single-junction thermophotovoltaic cells based on the device transport model

Xin-Miao Zhu(朱鑫淼), Min Cui(崔敏), Yu Wang(汪宇), Tian-Jing Yu(于添景),Jin-Xiang Deng(邓金祥), and Hong-Li Gao(高红丽)

Citation: Chin. Phys. B, 2022, 31 (**5**): 058801. DOI: 10.1088/1674-1056/ac4749
Journal homepage: http://cpb.iphy.ac.cn; http://iopscience.iop.org/cpb

What follows is a list of articles you may be interested in

Exploring alkylthiol additives in PBDB-T:ITIC blended active layers for solar cell applications

Xiang Li(李想), Zhiqun He(何志群), Mengjie Sun(孙盟杰), Huimin Zhang(张慧敏), Zebang Guo(郭泽邦), Yajun Xu(许亚军), Han Li(李瀚), Chunjun Liang(梁春军), Xiping Jing(荆西平)
Chin. Phys. B, 2019, 28 (**8**): 088802. DOI: 10.1088/1674-1056/28/8/088802

Efficient ternary organic solar cells with high absorption coefficient DIB-SQ as the third component

Hui-Xin Qi(齐慧欣), Bo-Han Yu(余泊含), Sai Liu(刘赛), Miao Zhang(张苗), Xiao-Ling Ma(马晓玲), Jian Wang(王健), Fu-Jun Zhang(张福俊)
Chin. Phys. B, 2018, 27 (**5**): 058802. DOI: 10.1088/1674-1056/27/5/058802

Sodium chloride methanol solution spin-coating process for bulk-heterojunction polymer solar cells

Tong-Fang Liu(刘统方), Yu-Feng Hu(胡煜峰), Zhen-Bo Deng(邓振波), Xiong Li(李熊), Li-Jie Zhu(朱丽杰), Yue Wang(王越), Long-Feng Lv(吕龙锋), Tie-Ning Wang(王铁宁), Zhi-Dong Lou(娄志东), Yan-Bing Hou(侯延冰), Feng Teng(滕枫)
Chin. Phys. B, 2016, 25 (**8**): 088801. DOI: 10.1088/1674-1056/25/8/088801

Improved performance of P3HT：PCBM solar cells by both anode modification and short-wavelength energy utilization using $Tb(aca)_3phen$

Zhuo Zu-Liang, Wang Yong-Sheng, He Da-Wei, Fu Ming
Chin. Phys. B, 2014, 23 (**9**): 098802. DOI: 10.1088/1674-1056/23/9/098802

MoO_3/Ag/Al/ZnO intermediate layer for inverted tandem polymer solar cells

Qing Jian, Zhong Zhen-Feng, Liu Yong, Li Bao-Jun, Zhou Xiang
Chin. Phys. B, 2014, 23 (**3**): 038802. DOI: 10.1088/1674-1056/23/3/038802

GeSn (0.524 eV) single-junction thermophotovoltaic cells based on the device transport model

Xin-Miao Zhu(朱鑫淼)[1], Min Cui(崔敏)[1,†], Yu Wang(汪宇)[2], Tian-Jing Yu(于添景)[1], Jin-Xiang Deng(邓金祥)[1], and Hong-Li Gao(高红丽)[1]

[1] *Faculty of Science, Beijing University of Technology, Beijing* 100124, *China*

[2] *Department of Physics, Faculty of Science, Kunming University of Science and Technology, Kunming* 650500, *China*

(Received 23 July 2021; revised manuscript received 15 November 2021; accepted manuscript online 31 December 2021)

Based on the transport equation of the semiconductor device model for 0.524 eV GeSn alloy and the experimental parameters of the material, the thermal–electricity conversion performance governed by a GeSn diode has been systematically studied in its normal and inverted structures. For the normal p^+/n (n^+/p) structure, it is demonstrated here that an optimal base doping $N_{d(a)} = 3(7) \times 10^{18}$ cm^{-3} is observed, and the superior p^+/n structure can achieve a higher performance. To reduce material consumption, an economical active layer can comprise a 100 nm–300 nm emitter and a 3 μm–6 μm base to attain comparable performance to that for the optimal configuration. Our results offer many useful guidelines for the fabrication of economical GeSn thermophotovoltaic devices.

Keywords: GeSn, thermophotovoltaic device, active layer, photovoltaic cell

PACS: 88.40.fc, 84.60.Rb, 02.60.–x, 78.40.Fy **DOI:** 10.1088/1674-1056/ac4749

1. Introduction

Over the past few decades, thermophotovoltaics (TPVs)[1–6] have received increasing interest due to their excellent characteristics such as high energy conversion efficiency, superior output power, compactness, etc. The need exists with TPV cells to increase their efficiency with narrow band gap (0.5 eV–0.7 eV)[7] engineered materials compatible with economical substrates. Compared with conventional TPV materials, GeSn provides a tunable narrow band gap (0.5 eV–0.66 eV) by controlling the Sn content in direct-transition semiconductors with increasing Sn concentration, higher carrier mobility and epitaxial fabrication for large-scale Si processes.[8] Therefore, these advantages of GeSn suggest the potential application of GeSn in TPV devices.

However, epitaxial growth of GeSn crystals is very challenging because of the huge lattice mismatch between Ge and α-Sn (14.7%), the surface segregation of Sn in Ge[9] and the extremely low equilibrium solubility of Sn in Ge ($\sim 1\%$).[10] Recently, many research groups have successfully fabricated high-quality GeSn epitaxial films[11–13] and GeSn photodetectors,[14,15] but photovoltaic research on GeSn is still in its initial stage. Conley *et al.*[8,16] have manufactured high-quality GeSn films on Si using a relaxed Ge buffer layer, which can be used in high-efficiency multi-junction PV and TPV cells. The relaxation of strain in GeSn alloys with a higher Sn content (12%) has been investigated by Kondratenko *et al.*,[17] with promising results for GeSn PV cell applications. Up to now, there have been few investigations into GeSn TPVs. It is thus urgent to study GeSn for TPV applications both theoretically and experimentally.

In this paper, based on the transport equation for semiconductor devices, we focus on studying the dependence of thermal radiation conversion performance on the active layer and black-body temperature using a 0.524 eV GeSn TPV cell as an ideal diode. Four concrete configurations, p–on–n and n–on–p stacks in normal and inverted form, were investigated and compared. The results of this work can offer many profitable guidelines for the development of related TPV cells.

2. Model and simulation

A previous report[18] stated that direct band gap GeSn (0.524 eV) with a Sn content of 10% has been fabricated; we use this as our study material. Four GeSn single-junction TPV cells with p^+/n, n^+/p, p/n^+, and n/p^+ structures, respectively, were studied. For each structure, an ideal diode was extracted from its practical condition as the device active layer. The effects of surface photonic reflection loss, front electrode shadowing and parasitic resistance on cell performance have been neglected in this work. On the basis of the classical photovoltaic cell model,[19] the current density (J)–voltage (V) characteristics are given as

$$J = J_{sc} - J_0 \left[\exp\left(qV/k_B T\right) - 1\right], \tag{1}$$

where q, T, and k_B denote the elementary charge, cell temperature and Boltzmann constant, respectively. J_{sc} can be derived as

$$J_{sc} = \int_0^{\lambda_m} q\phi\left(\lambda\right) QE\left(\lambda\right) \mathrm{d}\lambda, \tag{2}$$

†Corresponding author. E-mail: mcui@bjut.edu.cn

© 2022 Chinese Physical Society and IOP Publishing Ltd

where λ and λ_m are the incident wavelength and cutting wavelength, respectively. $\phi(\lambda)$ is the irradiation spectrum of incident light and $QE(\lambda)$ is the internal quantum efficiency, which can be found in the classical text of Sze and Mattis.[19] $\phi(\lambda)$ is described in terms of Plank-like black-body irradiation as

$$\phi(\lambda) = 2\pi c\lambda^{-4}\left[\exp\left(hc/\lambda k_B T_{BB}\right) - 1\right]^{-1}, \tag{3}$$

where h is the Plank constant, c is the speed of light and T_{BB} is the radiator temperature, which provides thermal radiation energy to be converted into electricity by the TPV cell. The optical absorption model of direct band gap materials is as follows:[20]

$$\alpha(\lambda) = \frac{2\pi\lambda q^2 (2m_r)^{3/2}}{n\varepsilon_0 (cm_0)^2 h^3}\left(h\nu - E_g\right)^{1/2}\langle|P_{cv}|^2\rangle, \tag{4}$$

where n is the refractive index, ε_0 is the vacuum permittivity constant, ν is the photonic frequency and m_0 is the electron rest mass. The conversion mass m_r can be derived from the electron effective mass m_e^* and the hole effective mass m_h^* as $(m_r)^{-1} = (m_e^*)^{-1} + (m_h^*)^{-1}$. P_{cv} is the optical transition matrix, and $\langle|P_{cv}|^2\rangle$ can be determined as

$$\langle|P_{cv}|^2\rangle = \frac{2m_0^2 E_g\left(E_g + \Delta\right)}{3m_e^*\left(E_g + 2\Delta/3\right)}, \tag{5}$$

where Δ and E_g, respectively, are the spin–orbit splitting energy and the band gap.

Taking the p–on–n configuration as an example, and assuming fully ionized doping, device J_0 can be derived from the specific active layer as

$$J_0 = \frac{qn_i^2 D_e}{N_a L_e}\left\{\frac{\sinh\left(W_E/L_e\right) + \dfrac{S_F L_e}{D_e\cosh\left(W_E/L_e\right)}}{\cosh\left(W_E/L_e\right) + \dfrac{S_F L_e}{D_e\sinh\left(W_E/L_e\right)}}\right\} + \frac{qn_i^2 D_h}{N_d L_h}\left\{\frac{\sinh\left(W_B/L_h\right) + \dfrac{S_B L_h}{D_h\cosh\left(W_B/L_h\right)}}{\cosh\left(W_B/L_h\right) + \dfrac{S_B L_h}{D_h\sinh\left(W_B/L_h\right)}}\right\}, \tag{6}$$

where n_i is the intrinsic carrier concentration of the host material, $N_{a/d}$ is the acceptor/donor concentration in the p/n-type layer and $L(D)_{e/h}$ is the minority electron (e)/hole (h) diffusion length (coefficient) in the p/n-type layer, $W_{E/B}$ is the thickness of the quasi-neutral region of the diode emitter/base and $S_{F/B}$ is the surface recombination rate at the front/back surface.

Following the Einstein relationship, $D_{e/h}$ can be expressed in terms of the electron/hole minority carrier mobility $\mu_{e/h}$ as $D_{e/h} = k_B\mu_{e/h}T/q$, and $\mu_{e/h}$ can be determined from the empirical Caughey–Thomas model[21] as

$$\mu_{e/h}\left(N_{d/a}\right) = \mu_{min,e/h} + \frac{\mu_{max,e/h} - \mu_{min,e/h}}{1 + \left[\dfrac{N_{d/a}}{N_{ref,e/h}}\right]^{\alpha_{e/h}}}, \tag{7}$$

where $\mu_{min,e/h}/\mu_{max,e/h}$ denotes the value of electron/hole minority carrier mobility at the exceedingly low (high) doping density, $\alpha_{e/h}$ is the suggested fitting parameter and $N_{ref,e/h}$ represents the doping concentration at which the mobility is decreased to half the value it reaches for low doping at room temperature. $L_{e/h}$ in Eq. (6) is given as

$$L_{e/h} = \sqrt{D_{e/h}\tau_{e/h}}. \tag{8}$$

Considering radiation recombination, trap-assisted recombination (the Shockley–Read–Hall mechanism) and Auger recombination, the minority carrier lifetime $\tau_{e/h}$ can be expressed as

$$1/\tau_{e/h} = B_{opt}N_{a/d} + 1/\tau_{SRH,e/h} + \Lambda N_{a/d}^2, \tag{9}$$

where B_{opt}, $\tau_{SRH,e/h}$, and Λ are the radiation recombination coefficient, trap-assisted recombination lifetime and Auger recombination coefficient, respectively.

Therefore, after obtaining the J–V characteristics of the photovoltaic device and combining it with the total power σT_{BB}^4, where σ is the Stefan–Boltzmann constant, η for the TPV cell can be obtained. Table 1 shows the simulation parameters derived from experimental data used in this work.

Table 1. Some model parameters used in simulation.

Parameter	Value	Reference
n_i	5.23×10^{14} cm^{-3}	[22]
B_{opt}	6.41×10^{-14} cm^3·s^{-1}	[23]
Λ	1.1×10^{-31} cm^6·s^{-1}	[24]
$\tau_{SRH,e/h}$	2 μs	[25]
$\mu_{max,e}/\mu_{max,h}$	3895/2505 cm^2·V^{-1}·S^{-1}	[26,27]
$\mu_{min,e}/\mu_{min,h}$	641/175 cm^2·V^{-1}·S^{-1}	[26,27]
$N_{ref,e}/N_{ref,h}$	$6.33/9.33\times10^{16}$ cm^{-3}	[26,27]
α_e/α_h	1.04/0.9	[26,27]
m_e^*	$0.98m_0$	[28]
m_h^*	$0.49m_0$	[28]
Δ	0.35 eV	[29]
S_F/S_B	10^5 cm·s^{-1}	[30]

3. Results and discussion

Generally, the specific structure of a diode active layer can be constructed in the p–on–n or n–on–p configuration. Depending on the highly doped layer in the front (emitter) or rear (base) layer of diode, a normal or inverted structure can be further obtained for each configuration. To reveal the electricity generation controlled by the active layer, taking the doping profile at 10^{19} (10^{17}) cm^{-3} for the highly (lightly) doped layer, we have systematically researched the thickness evolution of the active layer on power conversion efficiency with a T_{BB} of 1500 K. The calculated results for the p–on–n configuration are shown in Fig. 1. It can be observed in Fig. 1(a) that with increasing thickness of the emitter, η demonstrates only a slight improvement initially and then a rapid decline. As

the base thickness increases, η increases rapidly then slowly. As described in Fig. 1(b), when the base thickness is 15 μm, the emitter increases to 0.09 μm, which gives the maximum conversion efficiency. Meanwhile, figure 1(c) shows that with increasing thickness of the base, η is enhanced from steeply increasing to flat and then increases to saturation; when the base is 5.4 μm thick a suboptimum η of 5.17% is obtained. We found that the cell showed higher efficiency with a thinner emitter and a thicker base, because the emitter plays a major role in the conversion efficiency. The emitter region can easily absorb high-energy photons and has a very small penetration depth, while the base region can more easily absorb long-wavelength photons and has a larger penetration depth. Moreover, the smaller thickness of the optimal emitter can be ascribed to a shorter minority carrier diffusion length due to the higher doping concentration in the emitter region. More significantly, in contrast to the optimum structure, the employment of quite a few suboptimal configurations is not remarkably degrading. From the viewpoint of designing an economical structure using fewer materials, a suboptimal structure can be a better choice.

In comparison with p^+/n, the results for the p/n^+ configuration are different, as shown in Fig. 1(d). As the emitter thickness increases, η improves initially and then decreases, and with increasing base thickness, η displays an initial rapid enhancement and then tends to be stable. Specifically, as can be seen in Fig. 1(e), the critical emitter thickness is 0.54 μm. Figure 1(f) shows that the base thickness with a tendency to increase to saturation is approximately 3.6 μm, and this presents a suboptimum η of 4.24%. In contrast to the optimal normal configuration, the entire cell thickness is reduced. Thus, the degradation of the absorption spectrum results in a decrease of η. For the inverted case, there is an increase in the optimum emitter thickness compared with the normal configuration. Physically, when reducing the doping profile of a device emitter, enlargement of the minority diffusion length L_e requires a thicker emitter.

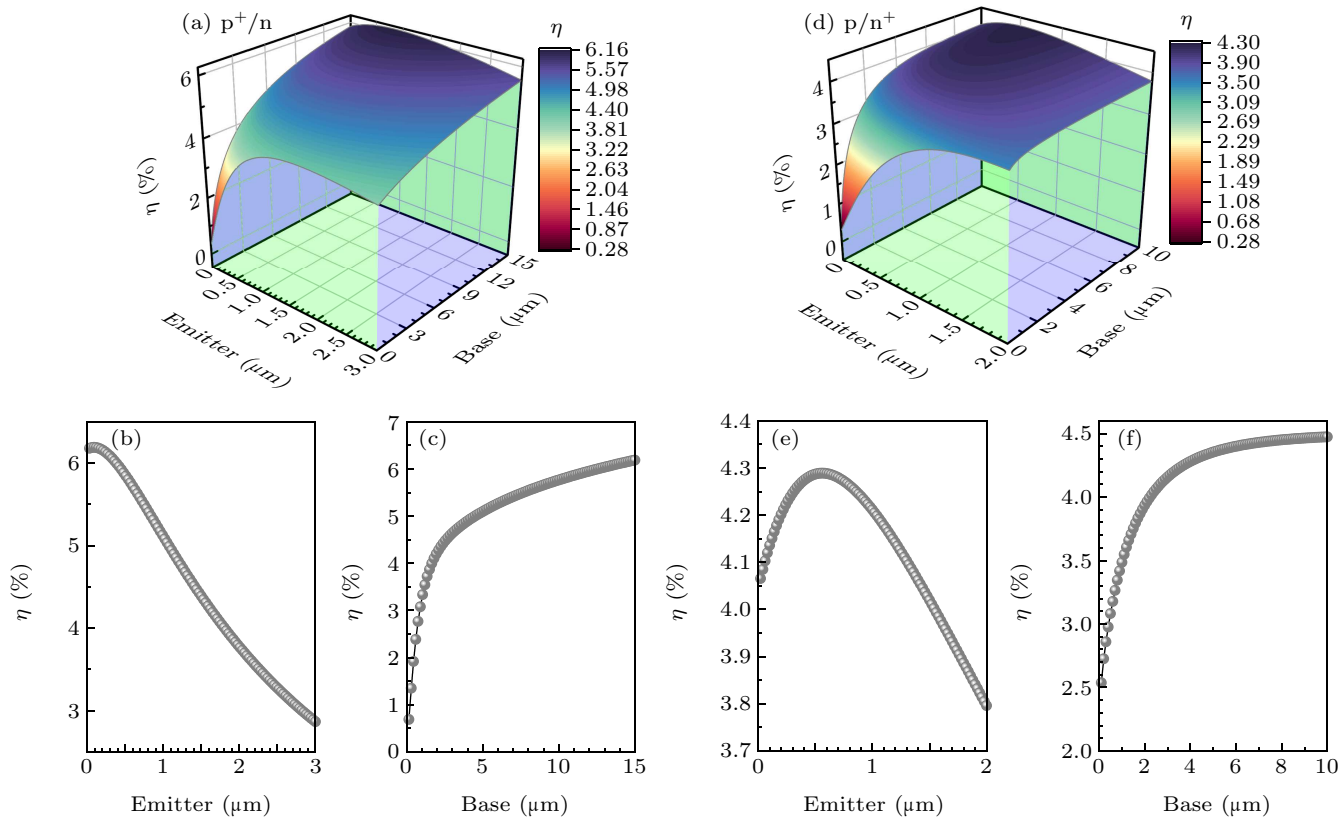


Fig. 1. Efficiency versus active layer thickness for p^+/n (a) and p/n^+ (d) configurations. For p^+/n and p/n^+ structures, the base thickness respectively is 15 μm (b) and 10 μm (e), η versus the emitter thickness; the emitter thickness respectively is 0.09 μm (c) and 0.54 μm (f), η versus the base thickness.

The n–on–p configuration as a function of active thickness is schematically described in Fig. 2. The dependence of η on the active layer thickness for the n^+/p device is shown in Fig. 2(a). With increasing emitter thickness, a peak value of η is observed, and as the base thickness increases, η displays an initial rapid increase and then tends to saturation, which is consistent with the normal p^+/n structure. It can be observed in Fig. 2(b) that when the base thickness is 12 μm, a critical emitter thickness of 0.024 μm is observed, which gives the maximum value of η. Figure 2(c) shows that when the base thickness increases to about 3.48 μm, a suboptimal η of 4.59% is achieved. The results can be understood as fol-

lows: since μ_e in the p-type emitter is smaller than μ_h in the n-type base, promoting the collection of minority electrons in the front layer, the resulting small L_e requires a thinner emitter. To compensate for the absorption loss caused by the thinner emitter, the base thickness should be appropriately enlarged for better spectral utilization. Compared with the n^+/p configuration, the results for the n/p^+ structure are diverse. As depicted in Fig. 2(d), with increasing emitter thickness, an initial increase and then a reduction in η was observed. To be specific, η is plotted as a function of the emitter thickness in Fig. 2(e), where the optimum emitter thickness is 0.39 μm, and as shown in Fig. 2(f) the base thickness tends to increase to saturation at approximately 2.48 μm, giving a suboptimal η of 4.04%.

In contrast to Figs. 1 and 2, we can see that the output performance of the inverted configuration is inferior to the normal one, and the p^+/n structure shows an optimal conversion efficiency. Physically, for the p^+/n construction, a higher minority carrier (electrons) mobility in the highly doped emitter makes it easier to collect photogenerated charge carriers. In the normal p^+/n construction, a reasonable active layer can be composed of a 100 nm–300 nm emitter and a 3 μm–6 μm base. These results for the configuration and active layer thickness can give useful guidelines for the GeSn TPV cell experiment.

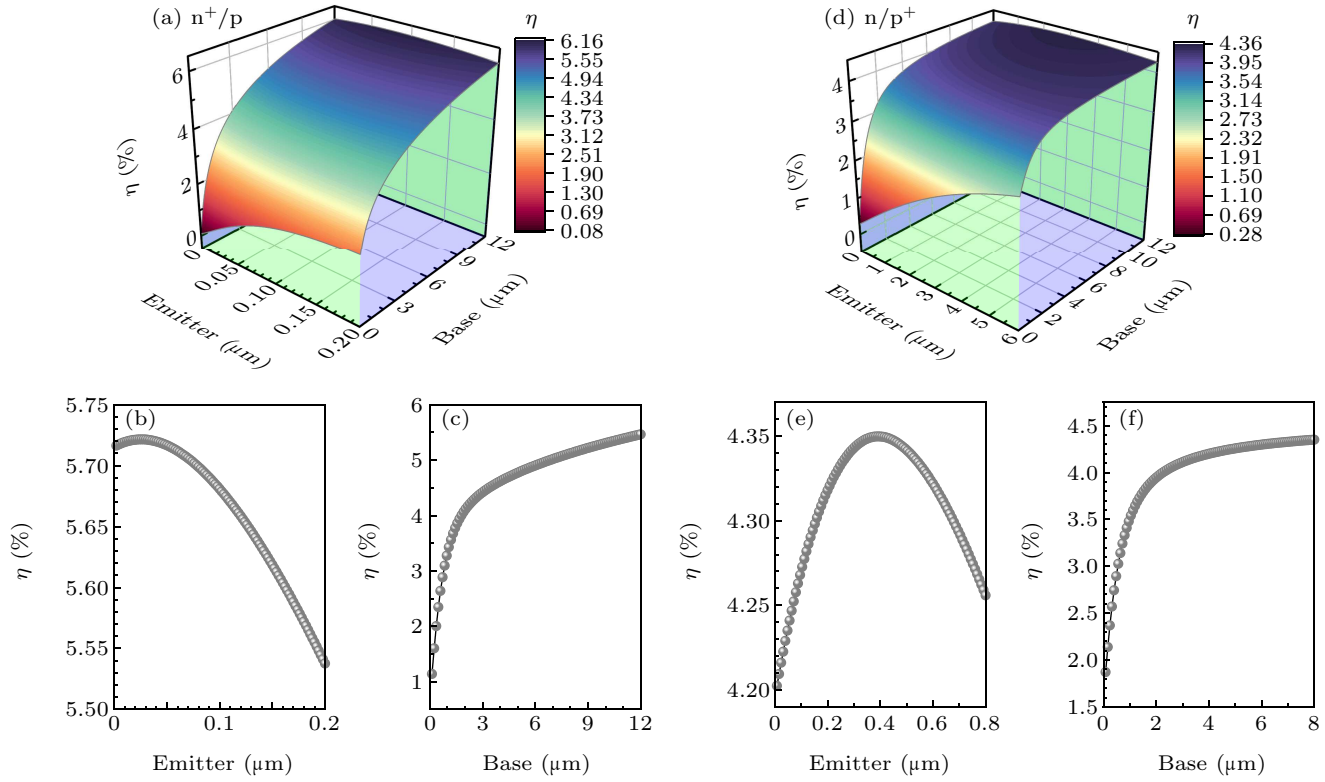


Fig. 2. Active layer thickness-dependent efficiency for n^+/p (a) and n/p^+ (d) structures. For n^+/p and n/p^+ configurations, the base thickness is 12 μm (b) and 8 μm (e), respectively, the emitter thickness-dependent η; the emitter thickness is 0.024 μm (c) and 0.39 μm (f), respectively, the base thickness-dependent η.

To further reveal the doping versus cell output characteristic, we can tune $N_{d(a)}$ in the lightly doped layer of the optimal configuration. The evolution of J_0 and J_{sc} with doping level is schematically displayed in Fig. 3. As shown in Fig. 3(a), with increasing doping, J_0 presents an initial dramatic reduction and then tends to saturation. The degradation of J_0 can be attributed to the inverse relationship between the doping concentration and J_0 (as shown in Eq. (6)). As can be seen from Fig. 3(b), J_{sc} for the p^+/n (n^+/p) configuration decreases from 14.53 (14.47) A·cm^{-2} for $N_{d(a)} = 1 \times 10^{17}$ cm^{-3} to 13.72 (14.09) A·cm^{-2} for $N_{d(a)} = 9 \times 10^{18}$ cm^{-3}. In the same doping range, J_{sc} for the inverted structure decreases from 13.83 (14.01) A·cm^{-2} with $N_{d(a)}$ of 1×10^{17} cm^{-3} to 13.07 (12.81) A·cm^{-2} with $N_{d(a)}$ of 9×10^{18} cm^{-3} for the p/n^+ (n/p^+) configuration. The weak degradation for each structure can be ascribed to the reduction of $\tau_{e/h}$ due to the increased doping. Thus, a reasonable doping level would improve TPV electricity generation.

Meanwhile, the corresponding characteristics of V_{oc}, fill factor (FF), and η as a function of the doping profile in the lightly doped layer for the optimum construction are evaluated in Fig. 4. Figure 4(a) shows that V_{oc} improves initially and then tends to be stable with increased doping. Specifically, V_{oc} for the p^+/n structure can be increased from 0.19 V for $N_d = 1 \times 10^{17}$ cm^{-3} to 0.27 V for $N_d = 6 \times 10^{18}$ cm^{-3} and then slightly diminishes, while V_{oc} (≈ 0.26 V) for the n^+/p configuration manifests extreme enhancement in the initial stage and then saturates at a higher doping level. As shown in Fig. 4(b),

with variation in doping level, FF is highly consistent with the observed V_{oc}. Consequently, η shows a distinct augmentation accompanying the upgraded doping in Fig. 4(c). For the p^+/n (n^+/p) construction, η displays an initial observable improvement when doping in the base region increases from 1×10^{17} cm^{-3} to 3 (7) $\times10^{18}$ cm^{-3}, for which a maximum η can be observed. A further increase in doping induces a slight reduction in η. These results are similar to the literature results for the 0.53 eV GaInAsSb TPV diode described by Wang and Lou.[31] For the p/n^+ (n/p^+) construction, η slowly improves from 4.28% (4.34%) with $N_{d(a)} = 1\times10^{17}$ cm^{-3} to 8.62% (8.49%) with $N_{d(a)} = 9\times10^{18}$ cm^{-3}. Under the same doping profile, the conversion efficiency of the normal construction is higher than that of the inverted one, which can be attributed to sufficient utilization of the spectrum due to the improved active layer thickness in the normal structure. Hence, with increasing doping, the enhancement of η is dominated by the increasing V_{oc}.

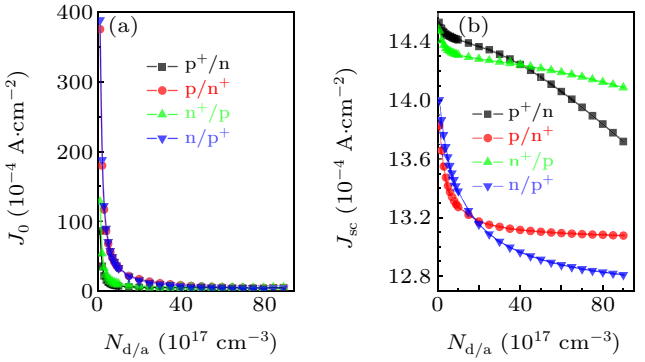


Fig. 3. The J_0 (a) and J_{sc} (b) of the optimum configurations versus the doping concentration in the lightly doped layer.

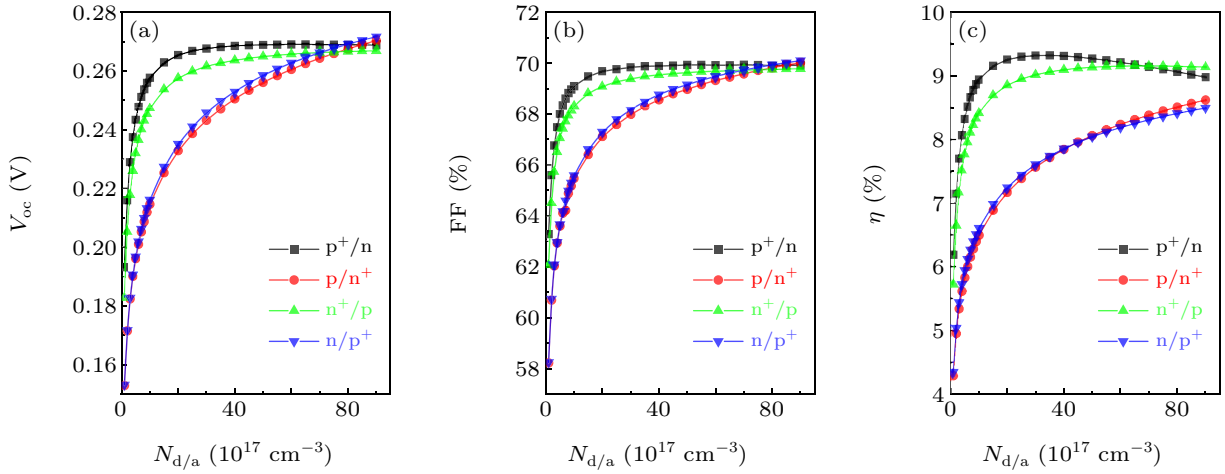


Fig. 4. The V_{oc} (a), FF (b), and η (c) of the optimum configurations versus the doping concentration in the lightly doped layer.

Since the radiation characteristic of an intermediate radiator can be controlled by artificial engineering, it is worth evaluating the potential effect of radiator temperature on device output performance of the optimal configuration. Figure 5 shows the photon flux (a) as a function of wavelength at different T_{BB}, and J_{sc} (b), V_{oc} (c), FF (d), POD (e), and η (f) versus the variation of T_{BB} for our considered configurations have been studied. As can be seen from Fig. 5(a), with increasing T_{BB}, the photon flux displays remarkable enhancement and a blue shift of the radiation peak was observed. In addition, GeSn (0.524 eV) with a cutoff wavelength of 2.36 μm was observed in the near-infrared band where it can capture most thermal radiation of photons from a black-body at 1500 K; this would facilitate the use of GeSn material in TPV cell applications. Figure 5(b) shows that J_{sc} shows exponential enhancement with the increasing T_{BB}. To be specific, J_{sc} improves from 1 A·cm^{-2} for $T_{BB} = 1000$ K up to 170 A·cm^{-2} for $T_{BB} = 2500$ K, which can be attributed to the enhancement of photon flux owing to the increased T_{BB}. Both V_{oc} and FF for each structure display evident improvement with the upgraded T_{BB}. For the p^+/n construction, V_{oc} (FF) in Figs. 5(c) and 5(d) increases from 0.12 V (53.87%) for $T_{BB} = 1000$ K up to 0.26 V (69.13%) for $T_{BB} = 2500$ K. The enlargement of V_{oc} can be understood because the increasing T_{BB} results in improved carrier collection, which can improve the band state, further leading to the band-filling effect[31,32] and slight augmentation of V_{oc}. For the normal structure V_{oc} is invariably larger than for the inverted one, which can be attributed to the smaller J_0 for the normal one. The improvement of FF can be attributed to the increased T_{BB}, and is derived from the empirical formula[33] $\mathrm{FF} = [V_{oc} - \ln(V_{oc}+0.72)]/(1+V_{oc})$. Figure 5(e) shows that POD displays exponential improvement with increasing T_{BB} due to the combined effect of J_{sc}, V_{oc}, and FF (POD = $J_{sc}\times V_{oc}\times$ FF). Moreover, η of the p^+/n (n^+/p) configuration increases from 1.22% (1.07%) for $T_{BB} = 1000$ K to 14.05% (13.28%) for $T_{BB} = 2500$ K; in the same T_{BB} range, η for the n/p^+ (p/n^+) configuration increases from 0.65% (0.69%) to 10.46% (10.89%), as shown in Fig. 5(f). Accordingly, an almost linear increase in η was observed, presenting a 12–16-fold improvement and revealing the significance of

controllable T_{BB} for TPV devices.

We know that surface recombination is a very important parameter for TPV cells. To reveal the potential effect of surface recombination rates, using the p^+/n configuration as an example, we have depicted TPV performance parameters versus the variables S_B and S_F in Fig. 6, where S_B and S_F of the optimal structure are equivalent to a T_{BB} of 1500 K. In Fig. 6(a), it is obvious that the concerned η varies when the value of $S_{F/B}$ is in the range of 10^3 cm·s^{-1}–10^7 cm·s^{-1}. The analogous behavior for other parameters such as J_{sc}, V_{oc}, FF, and POD is also shown in Fig. 6. Cell performance would be improved with decreasing $S_{F/B}$, In particular, cell performance decreases at high (10^7 cm·s^{-1}–10^{10} cm·s^{-1}) surface recombination rates, but low (10^1 cm·s^{-1}–10^3 cm·s^{-1}) surface recombination rates give a higher thermoelectric conversion performance, indicating the significance of good quality contacts in practical TPV applications. A feasible way to reduce $S_{F/B}$ is by passivating the surface of the device to remove the recombination resource formed by surface impurities; this is helpful for improving cell conversion efficiency.[34]

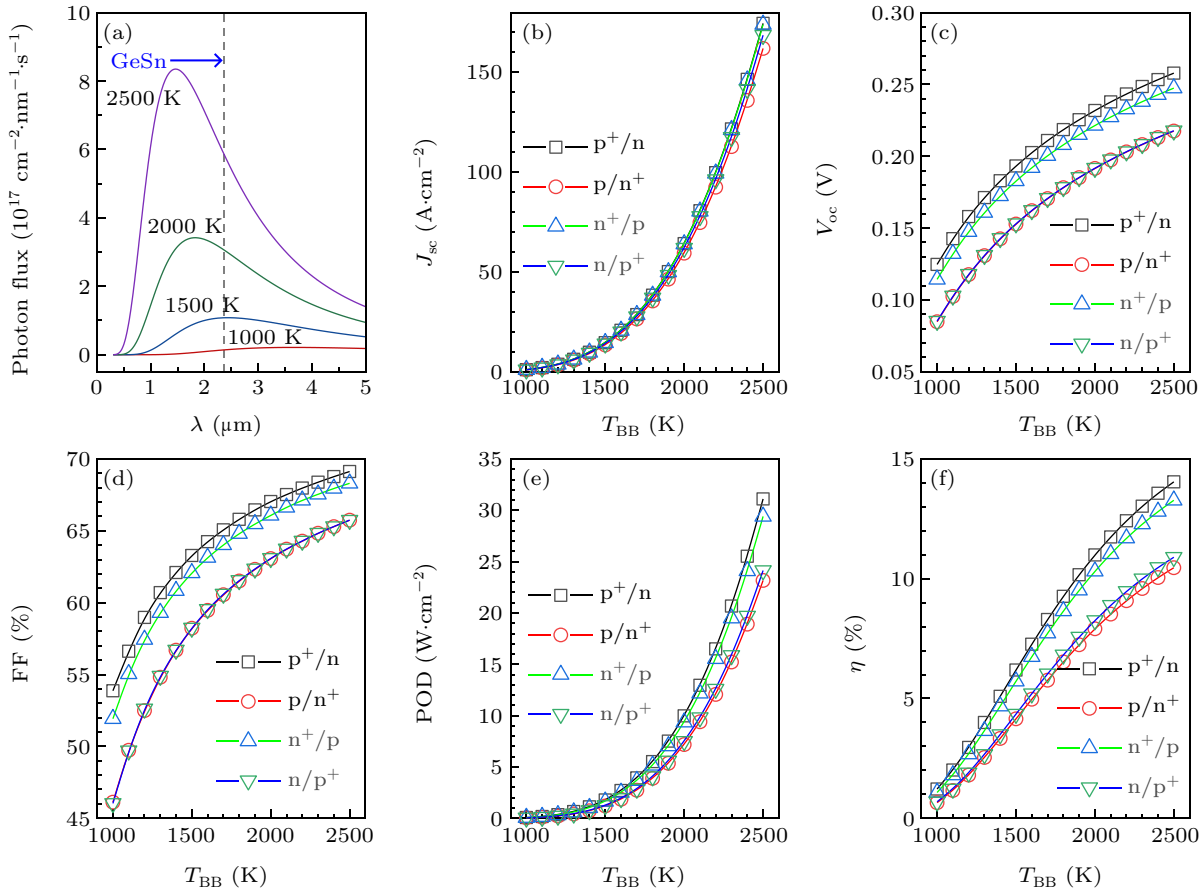


Fig. 5. Photon flux per unit wavelength at different T_{BB} (a), and dependence of the optimal structure J_{sc} (b), V_{oc} (c), FF (d), POD (e), and η (f) on various values of black-body illumination.

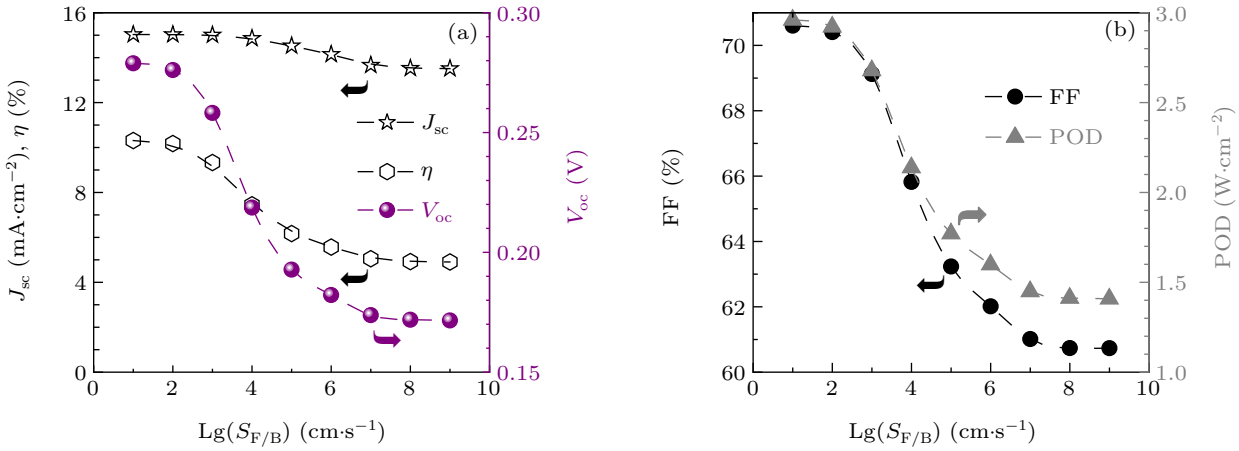


Fig. 6. Device performances of J_{sc}, V_{oc}, η (a) and FF, POD (b) with variation of $S_{F/B}$.

4. Conclusion

In this paper, we have systematically studied the effects of the active layer on the output performance of GeSn single-junction TPV cells with normal and inverted configurations. The results show that GeSn TPV cells with acceptable performance consisting of a 100 nm–300 nm emitter and a 3 μm–6 μm base with low device cost and the optimal p^+/n structure have been obtained. In the p^+/n (n^+/p) structure, there is an optimum base doping $N_{d(a)} = 3\ (7) \times 10^{18}$ cm^{-3}. Performance of the GeSn TPV cells can be improved by increasing the radiator temperature and decreasing surface recombination. The simulated results provide some useful guidelines for the fabrication of economical GeSn TPV devices.

Acknowledgment

Project supported by the Beijing Natural Science Foundation Program, China (Grant No. 4192016).

References

[1] Cakiroglu D, Perez J P, Evirgen A, Lucchesi C, Chapuis P O, Taliercio T, Tournié E and Vaillon R 2019 *Sol. Energy Mater. Sol. Cells* **203** 110190
[2] Omair Z, Scranton G, Pazos-Outón L M, Xiao T P, Steiner M A, Ganapati V, Peterson P F, Holzrichter J, Atwater H and Yablonovitch E 2019 *Proc. Natl. Acad. Sci. USA* **116** 15356
[3] Zhou Z, Jiang C, Huang H, Liang L and Zhu G 2020 *Energy* **210** 118503
[4] Liang T, Fu T, Hu C, Chen X, Su S and Chen J 2021 *Renew. Energy* **173** 942
[5] Fekadu M, Namkyu L, Geehong C, Taehwan K and Hyung C 2018 *Energies* **11** 2299
[6] Xu W, Liu Y, Tang L, Zhang Y and Xu C 2021 *Infrared Physics & Technology* **115** 103719
[7] Coutts T J 1999 *Renew. Sust. Energy Rev.* **3** 77
[8] Conley B R, Mosleh A, Ghetmiri S A, Naseem H A, Tolle J and Yu S Q 2013 *Conference Record of the IEEE Photovoltaic Specialists Conference* pp. 1346–1349
[9] Harwit A, Pukite P R, Angilello J and Iyer S S 1990 *Thin Solid Films* **184** 395
[10] Kaiser W and Thurmond C D 1961 *J. Appl. Phys.* **32** 115
[11] Lu Z H Y H, Wang Y S, Li C, Lin G Y, Chen S Y, Huang W and Wang J Y 2017 *Chin. Phys. B* **26** 116802
[12] Schwarz D, Funk H S, Oehme M and Schulze J 2020 *J. Electron. Mater.* **49** 5154
[13] Galluccio E, Mirabelli G, Harvey A, Conroy M, Napolitani E and Duffy R 2021 *Materials Science in Semiconductor Processing* **121** 105399
[14] Zhao N W, Kai Yu, Zhang X M, Li X L, Zheng J, Xue C L, Cheng B W and Li C B 2019 *Chin. Phys. B* **28** 128501
[15] Ghosh S, Lin K C, Tsai C H, Kumar H, Chen Q, Zhang L, Son B, Tan C S, Kim M, Mukhopadhyay B and Chang G E 2020 *Micromachines* **11** 795
[16] Conley B R, Naseem H, Sun G, Sharps P and Yu S Q 2012 *Photovoltaic Specialists Conference IEEE* 001189-001192
[17] Kondratenko S V, Hyrka Y V, Mazur Y I, Kuchuk A V, Dou W, Tran H, Margetis J, Tolle J, Yu S Q and Salamo G J 2019 *Acta Mater.* **171** 40
[18] Pham T, Du W, Tran H, Margetis J, Tolle J, Sun G, Soref R A, Naseem H A, Li B and Yu S Q 2016 *Opt. Express* **24** 4519
[19] Sze S M and Mattis D C 1970 *Phys. Today* **23** 75
[20] Basu P K 1997 *Theory of Optical Processes in Semiconductors - Bulk and Microstructures*
[21] Caughey D M and Thomas R E 1967 *Proc. IEEE* **55** 2192
[22] Paul J, Mondal C and Biswas A 2019 *Materials Science in Semiconductor Processing* **94** 128
[23] Auston D H, Shank C V and Lefur P 1975 *Phys. Rev. Lett.* **35** 1022
[24] Sermage B, Eichler H J, Heritage J P, Nelson R J and Dutta N K 1983 *Appl. Phys. Lett.* **42** 259
[25] Gaubas E, Bauža M, Uleckas A and Vanhellemont J 2006 *Materials Science in Semiconductor Processing* **9** 781
[26] Jacoboni C, Nava F, Canali C and Ottaviani G 1981 *Phys. Rev. B* **24** 1014
[27] Liu Z, Wen J, Zhang X, Li C, Xue C, Zuo Y, Cheng B and Wang Q 2014 *J. Phys. D: Appl. Phys.* **48** 445103
[28] Liu L, Liang R, Wang J and Xu J 2015 *Appl. Phys. Express* **3** 031301
[29] Chadi D J 1977 *Phys. Rev. B* **16** 790
[30] Virgilio M, Manganelli C L, Grosso G, Schroeder T and Capellini G 2013 *J. Appl. Phys.* **114** 243102
[31] Wang Y and Lou Y Y 2015 *Renew. Energy* **75** 8
[32] Wang Y, Zhang X, Zhang X and Chen N 2012 *Renew. Energy* **48** 231
[33] Green M A 1982 *Sol. Energy* **1** 5
[34] Donetsky D, Belenky G, Svensson S and Suchalkin S 2010 *Appl. Phys. Lett.* **97** 052108